Chapter 14

Silicon Oxycarbide Thin films and Nanostructures: Synthesis, Properties and Applications

Spyros Gallis, Vasileios Nikas and Alain E. Kaloyeros

Additional information is available at the end of the chapter

http://dx.doi.org/10.5772/66992

Abstract

Silicon oxycarbide (SiC_xO_y) has been extensively investigated due to its wide use in the Si semiconductor industry in applications that include low-k dielectrics, passivation layers, and etch-stop layers. Furthermore, SiC_xO_y research has been exploring its prospective use in numerous other technological usages, such as lighting, energy, and biological applications. The latter include white light-emitting materials, hydrogen storage materials, gas sensors, anode materials for lithium batteries, and biomedical devices. SiC_xO_y materials can intensively luminescence in a broad emission spectral range that spans the ultraviolet, the visible, and even the near-infrared spectrum, when doped with erbium. Herein, we present pertinent results on the material behaviors from chemically synthesized SiC_xO_y thin films and nanowires. Moreover, their light-emitting properties and underlying mechanisms for light emission are explored in conjunction with data from their thin film counterparts, which are also employed as baseline comparison metric. We further highlight major challenges and promises of such materials.

Keywords: silicon oxycarbide, SiC_xO_y, Si-O-C, Si-C-O, nanowires, thin films, luminescence, CVD, e-beam lithography, structural properties, optical properties, band tails, disorder

1. Introduction

In silicon (Si) complementary metal-oxide-semiconductor (CMOS) chip technology, silicon oxycarbide (SiC_xO_y) materials have been extensively employed to serve multiple purposes. For example, SiC_xO_y materials have been the focus of extensive study due to their applicability

as low-k dielectrics, passivation layers, and etch-stop layers to name a few [1, 2]. SiC_xO_y materials have also been the focus of studies due to their potential application in a plethora of other technological applications (e.g. light emission, energy, and bioapplications). In particular, they have been proposed as candidates for white light-emitting materials [3–5], filters, porous adsorbents, and catalytic supports [6, 7], as hydrogen storage materials [8], gas sensors [9], negative electrode materials for lithium batteries [10, 11], and in biomedical devices [12]. Additionally, it has been also shown that SiC_xO_y can be utilized as a host material to optically active impurities (rare earth ions). To this end, europium (Eu^{2+})-doped SiC_xO_y thin films synthetized by RF magnetron sputtering [13] as well as erbium (Er^{3+})-doped SiC_xO_y thin films for near-infrared (IR) emission at the commercially useful telecommunication wavelength of 1540 nm have been recently reported [14–16].

The fabrication of luminescent Si-based nanostructured materials for light emission applications is highly desirable, similarly to how Si-based nanophotonics has undergone great advancements in recent years [17, 18]. Due to the seamless integration of Si-based materials with process protocols and technologies developed for semiconductor CMOS technology, manufacturing costs and process complexity could be also reduced. Furthermore, the extreme down-scaling methods achieved by CMOS technology offer the opportunity to study new compelling properties owing to possible confinement effects in one (1D) or two (2D) dimensions (e.g., the reduction of exciton-phonon interactions, the increase of extraction efficiency of spontaneous emission, and suppression of Auger recombination) [19, 20]. Therefore, the functionality of such nanostructured materials and their devices can be employed in a ubiquitous way in light emission applications [21]. To this extent, SiC_xO_y nanowires (NWs) have been recently shown to exhibit strong room-temperature visible luminescence [22–24].

In parallel, the identification and elimination of potential obstacles that could deteriorate the luminescence efficiency of such materials (e.g., temperature and excitation power density) needs to be taken into consideration. Indeed, the luminescence efficiency is known to be influenced by environmental fluctuations in temperature and pump-power-density changes [25, 26]. These fluctuations can become critical in luminescence applications such as light-emitting diodes (LEDs). In these applications, the operating temperature and power density can reach respectively ~150°C and ~200 W/cm^2, thus greatly influencing the light output and color chromaticity.

Silicon oxycarbide films have been grown predominantly through low-temperature plasma-enhanced chemical vapor deposition (PECVD) using an array of silane-based precursors for the needs of semiconductor industry [27–30]. However, the incorporation of source precursor fragments and decomposition byproducts in the resulting films has led to the observation of enhanced stress levels and increased defect density, both of which have detrimental effects on the optical performance of resulting materials and device structures. Recently, Lin et al. prepared amorphous SiC_xO_y using a very high-frequency plasma-enhanced chemical vapor deposition (VHF-PECVD) technique [31]. The resulting films exhibited intense room-temperature blue luminescence, characteristic of Si-related neutral oxygen vacancy defect centers. Ryan et al. and Vasin et al. showed that a wide variety of SiC_xO_y with a continuous range of compositions could be produced by reactive RF-magnetron sputtering [32, 33]. Karakuscu et al. and Abbass et al. have reported sol-gel-prepared SiC_xO_y thin films [34, 35], while Vasin

et al. have reported a-SiC_xO_y:H thin films growth by low-temperature oxidation of carbon-rich a-Si_xC_y:H thin films [36].

Nevertheless, it is desirable to identify alternative deposition methods, which can inhibit or minimize processing induced structural and/or compositional damage to SiC_xO_y materials due to phase separation owing to the non-stoichiometric composition. Herein, key findings are summarized pertaining to the development of a thermal chemical vapor deposition (TCVD) strategy for the growth of SiC_xO_y thin films approximating the $SiC_xO_{2(1-x)}$ ($0 < x < 1$) stoichiometry for light emission applications [37, 38]. These studies led to the identification of a deposition process window for the growth of SiC_xO_y thin films with strong room-temperature light emission [3]. Additionally, we present the findings pertaining to room-temperature visible photoluminescence (PL) from SiC_xO_y sub-100-nm nanowire materials fabricated by electron beam lithography (EBL) and reactive ion etching (RIE). These metal-free non-toxic Si-based nanostructured materials may offer an alternative and environmentally friendly pathway toward efficient visible light-emitting materials and devices.

2. Synthesis and fabrication of silicon oxycarbide thin films and nanostructures

2.1. SiC_xO_y materials grown by thermal chemical vapor deposition: composition control

SiC_xO_y thin films and their nanostructures are deposited on Si(100) or SiO_2 substrates in a hot-wall quartz tube reactor by thermal CVD at 800°C. A single source oligomer (2,4,6-trimethyl-2,4,6-trisila-heptane ($C_7H_{22}Si_3$)) is utilized as the source precursor for silicon and carbon atoms and ultra-high purity oxygen (O_2) and argon (Ar)/nitrogen (N_2) are also employed as co-reactant and dilution gases. The composition of the resulting amorphous $SiC_xO_{y\leq1.73}$ ($0.11 < x < 0.65$) thin films is regulated by modifying the oxygen flow rate and, hence, the oxygen partial pressure in the reaction zone. The films are deposited onto three types of substrates: single-crystal silicon (c-Si) (100), for composition, structural and optical analysis; double-polished intrinsic Si and high-quality UV transparent fused silica, for infrared and optical studies. A subset of the as-deposited SiC_xO_y films was annealed for 1 h in different ambient (e.g., O_2, Ar, N_2, or forming gas (FG, 5% H_2 and 95% N_2)) at temperatures in the range from 500 to 1100°C. Detailed description of the deposition and annealing processes can be found elsewhere [37, 38]. The resulting samples were subsequently employed in a comparative analysis of as-deposited and post-annealed films to determine the effects of thermal treatment on film structural and optical properties as well as their photoluminescence performance.

Rutherford backscattering spectroscopy (RBS) and X-ray photoelectron spectroscopy (XPS) were employed to determine the Si, C, and O content in the SiC_xO_y materials and they were separated in three different classes, defined by their composition: SiC-like ([O] < 5 at.%), Si-C-O, and SiO_2-like ([C] < 5 at.%). The compositional evolution of the SiC_xO_y thin films was plotted in the Si-C-O ternary diagram of **Figure 1a** along with the $SiC_xO_{2(1-x)}$ ($0 < x < 1$) line, with the latter representing stoichiometric silicon oxycarbide without any excess of carbon. The upper and lower limits in $SiC_xO_{2(1-x)}$ correspond to SiC and SiO_2, for, respectively, x = 1 and 0 [39, 40].

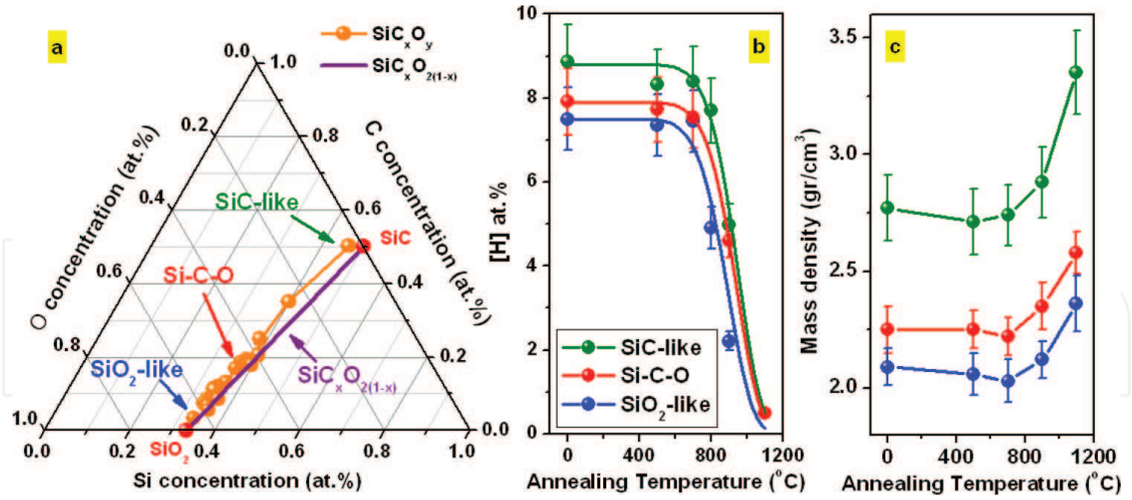

Figure 1. (a) Si-C-O ternary diagram with the compositions of as-deposited (AD) silicon oxycarbide (SiC_xO_y) materials, (b) NRA hydrogen depth profiles of the as-deposited SiC_xO_y and (c) mass density of $SiC_xO_yH_z$ films [22, 37].

As is shown in **Figure 1a**, the composition of the thermal CVD-grown SiC_xO_y was properly tailored to closely follow the pure stoichiometric oxycarbide formula over the whole range of the synthesis process parameters. The $SiC_xO_{2(1-x)}$ behavior observed in the samples produced herein suggests the substitution of two divalent oxygen atoms by one tetravalent carbon atom as the C concentration in the SiC_xO_y materials increases. The latter will be further discussed in Section 3.1. Furthermore, the observed small deviation from the stoichiometric $SiC_xO_{2(1-x)}$ trend suggests that there is much less excess of C compared to non-stoichiometric compositions reported for SiC_xO_y with SiC/SiO_2 phases and free carbon, as it is shown in **Figure 1** of reference [39].

Due to the presence of methyl groups in the CVD reactants, it is expected to have hydrogen atoms in the grown silicon oxycarbide thin films whose concentration cannot be quantified by the RBS or XPS techniques. Instead, the nuclear reaction analysis (NRA) was conducted by using the $^{15}N + {}^{1}H \rightarrow {}^{12}C + {}^{4}He + \gamma$-ray resonant nuclear reaction at 6.835 MeV [41]. **Figure 1b** shows the NRA-derived hydrogen concentration measurements of the silicon oxycarbide films as a function of post-deposition annealing temperature T_a [37]. After the 900°C annealing step, the hydrogen content is significantly reduced to 5, 2.2, and 4.5 at.%, respectively, for the SiC-like, Si-C-O, and SiO_2-like samples. For annealing temperatures above 1000°C, the hydrogen content was not detectable (>1 at.%) in all three different types of samples.

The mass density ρ (g/cm^3) of thin films was calculated using the elemental compositions determined by RBS and XPS and the thicknesses measured by scanning electron microscope (SEM) by employing the following equation:

$$\rho = \frac{D \times 10^{15}}{d} \times 1.66 \times 10^{-24} \frac{(A_{Si} + xA_C + yA_O + zA_H)}{(1 + x + y + z)} \quad (gr/cm^3) \tag{1}$$

where D is the thickness in rump units, which is related to the planar density, d is the film thickness, A_{Si}, A_C, A_O, and A_H are the atomic weights of Si, C, O, and H, respectively, and x, y, and z are the normalized fractional contents, respectively, of C, O, and H.

http://dx.doi.org/10.5772/66992

The density of the silicon oxycarbide films was observed to increase with higher annealing temperature, due at least partly to the reduction in hydrogen concentration, as shown in **Figure 1c**. More specifically, the densities of the as-deposited films are 2.8, 2.2, and 2.1 for, respectively, SiC-like, Si-C-O, and SiO_2-like films. After annealing at 1100°C, the densities were measured to be significantly higher, with values of 3.3, 2.6, and 2.4 g/cm^3 for, respectively, SiC-like, Si-C-O, and SiO_2-like films.

2.2. Nanofabrication of silicon oxycarbide nanostructures

SiC_xO_y nanostructured systems were fabricated by electron beam lithography and reactive ion etching, namely periodically ordered sub-100-nm nanowire arrays. A representation of the baseline nanofabrication scheme of the SiC_xO_y NW arrays is schematically depicted in **Figure 2**. Following the synthesis of SiC_xO_y thin films, negative hydrogen silsesquioxane (HSQ) (6% HSQ in methyl-isobutyl-ketone solvent) resist is spun onto SiC_xO_y wafer pieces—deposited on Si (100)—at 1000 rpm, followed by a bake procedure for 4 min at 80°C. Line patterns are exposed using electron beam lithography and then the resulting wafer piece is developed in a chemical solution bath (low concentration (2.38%) of tetramethylammonium hydroxide (TMAH) developer), yielding 2D-nanowire HSQ patterns. The HSQ patterns then underwent a hardening annealing process in Ar/N_2 ambient at 500°C, followed by a fluorine-based (e.g., combination of CHF_3 and CF_4 gases) anisotropic RIE to transfer the pattern into the SiC_xO_y thin films. The HSQ residue is then removed by wet etching in buffered hydrofluoric (BHF) acid, resulting in periodically well-defined NWs [22].

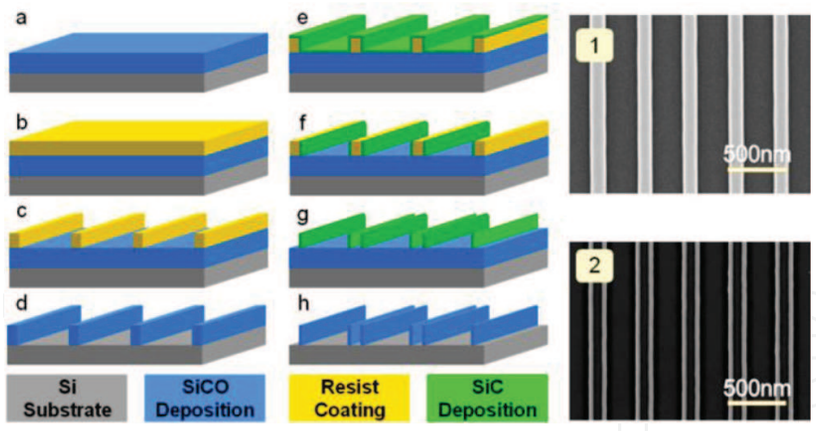

Figure 2. (a–d) Fabrication steps of the SiC_xO_y nanowires (NW) using lithography and RIE. The final NW arrays are shown in SEM image 1 and (e–h) fabrication steps of the SiC_xO_y nanowire (NW) arrays using the SIT method by SiC conformal deposition on the resist followed by RIE to open the SiC top layer, wet etch to remove the resist, and RIE. The final NW arrays made by SIT are shown in SEM image 2.

Pertaining to the NW fabrication, certain samples underwent a sidewall image transfer (SIT) process which was performed by conformal deposition of a thin silicon carbide (SiC) hard mask (sidewall layer) on the patterned photoresist followed by anisotropic RIE [23]. This allowed for a significant reduction of the critical dimensions as, during the SIT process, the NW width is defined by the thickness of the SiC layer rather than the resolution of the

lithography step. The SiC_xO_y NWs underwent different post-fabrication thermal treatments for up to 2 h at annealing temperatures in the range of 50–700°C in Ar, O_2, or forming gas (5% H_2 and 95% N_2) atmospheres.

3. Bonding configuration of silicon oxycarbide materials and nanowires

3.1. Fourier transform infrared spectroscopy (FTIR) characterization of silicon oxycarbide thin films

Figure 3a shows the Fourier transform infrared spectroscopy (FTIR) data of SiC_xO_y thin films in the 400–1700-cm^{-1} range. The spectra are characterized by three absorption bands and a shoulder assigned to the Si-O-C rocking, Si-C stretching, and Si-O transverse and longitudinal-stretching vibration modes, centered at, respectively, ~440, ~800, ~1000, and ~1150 cm^{-1} [22, 37, 38].

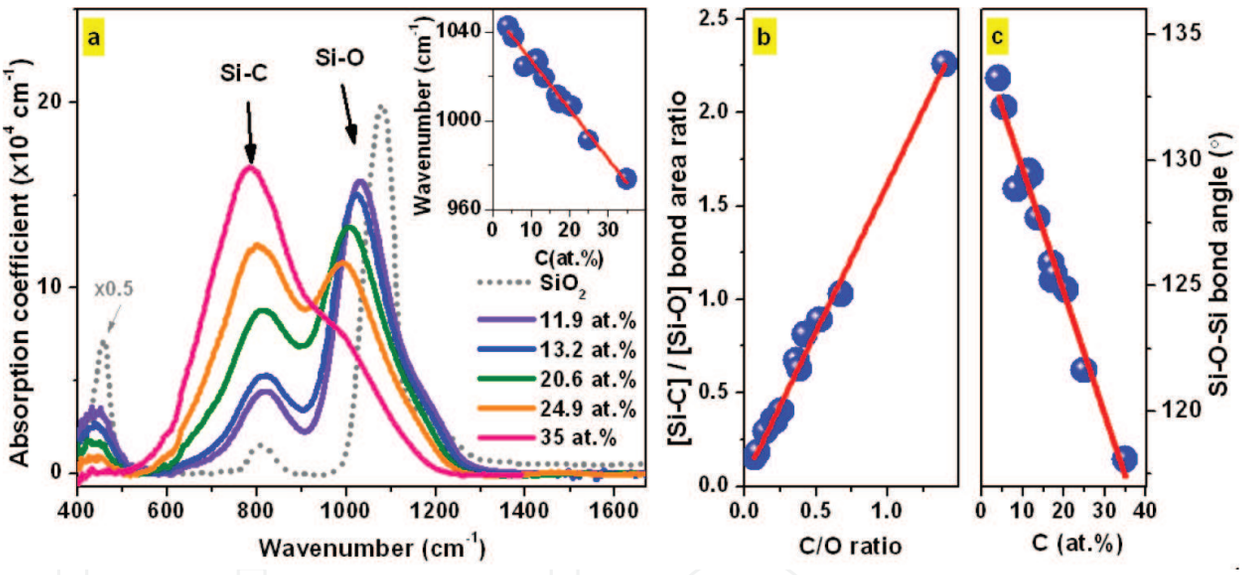

Figure 3. (a) The FTIR absorption spectra of the AD SiC_xO_y and SiO_2 control in the 400–1700 cm^{-1} range. The peak positions of the AD SiC_xO_y appear red-shifted compared to the SiO_2 control, due to the incorporation of less electronegative C, (b) the [Si-C]/[Si-O] bond-area ratio plotted as a function of the C/O content ratio showing a linear increase with increasing C/O and (c) the Si-O-Si bond angle of the bridging O atom in the SiC_xO_y [22].

More specifically, the Si-O-C vibration mode (~440 cm^{-1}) is caused by the ≡Si-O-Si≡ rocking mode due to out-of-plane motion of O in $O_{(3-x)}C_x$≡Si-O-Si≡$C_yO_{(3-y)}$ and is unaffected by the Si-O-Si-bridging bond-angle variation [42–45]. For samples with C content higher than 20 at.%, the density of ≡Si-O-Si≡-bonding groups decreased significantly, as dictated by the $SiC_xO_{2(1-x)}$ stoichiometry, suggesting that the backbone-bonding network related to the SiO_4 tetrahedral in SiC_xO_y changed toward SiC-like structures with significant presence of SiC_4 tetrahedral. The replacement of O atoms by C atoms with increasing C content in films is reflected in the monotonic increase of the bond area ratio of [Si-C] and [Si-O] as clearly depicted in **Figure 3b**.

http://dx.doi.org/10.5772/66992

Additionally, incorporation of the less electronegative C atoms leads to a reduced Si-O-Si bond angle between tetrahedral (see **Figure 3c**) [30, 44]. As a result, the density of the as-grown films is expected to increase with increasing C content, which is in agreement with the density values shown in Section 2.

Figure 4 displays the FTIR spectra collected in the range from 400 to 2300 cm^{-1} for the three classes of as-deposited silicon oxycarbide materials and for their annealed counterparts at 900 and 1100°C [37].

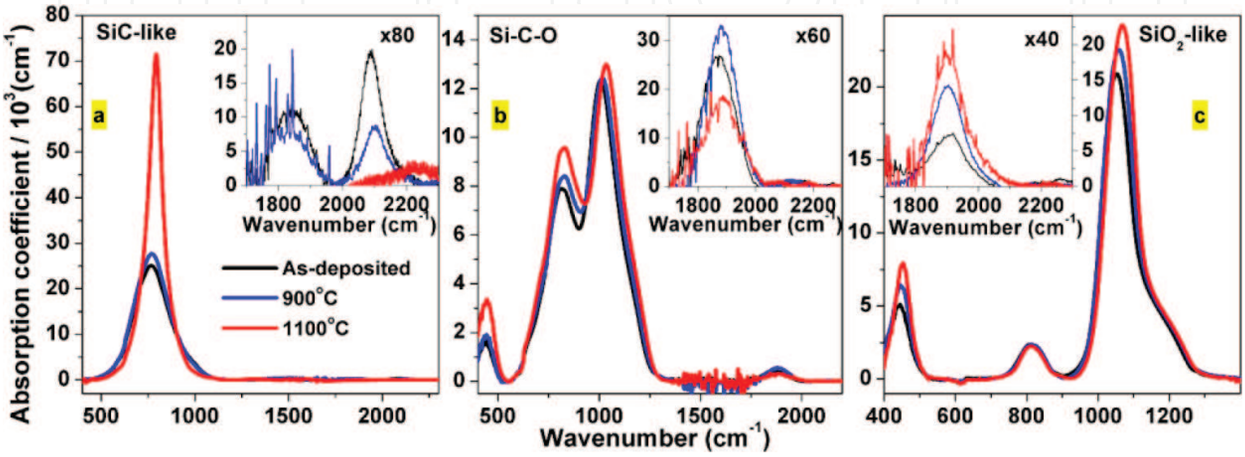

Figure 4. IR absorption spectra for the as-deposited, 900°C-, and 1100°C- annealed (a) SiC-like, (b) Si-C-O, and (c) SiO_2-like samples [37].

Deconvolution of the FTIR spectra reveals several bonding components in the as-deposited SiC_xO_y material systems [30, 37, 45, 46]. In particular, the deconvolution of the absorption bands in the range of 400–1400 cm^{-1} for the SiC-like film indicates the presence of a weak C-H mode at ~530 cm^{-1}, a major Si-C-stretching absorption mode at ~764 cm^{-1}, and a shoulder assigned to the Si-O-stretching mode at ~960 cm^{-1}. The hydrogen-related absorption bands (Si-H and C-H) are located at ~2100 and 2900 cm^{-1}, respectively. Finally, the absorption observed at ~1846 cm^{-1} is attributed to a C-O-stretching mode.

As seen in **Figure 4b**, the IR spectrum of Si-C-O film has three characteristic absorption band regions, originating from the Si-C and Si-O functional groups [37]. In comparison to the SiC-like matrix films, a new absorption peak is seen at ~440 cm^{-1}, attributed to the Si-O-C vibration mode discussed above. The IR region from 600 to 1300 cm^{-1} is broader compared to that in the SiC-like films, and its deconvolution shows the presence of four peaks centered at 663, 816, 1002, and 1114 cm^{-1} attributed to Si-C-H, Si-C stretching, and to the transverse optical (TO) and longitudinal optical (LO) asymmetric Si-O-stretching modes, respectively. Compared to the SiC-like films, the position of the Si-C absorption peak shifted from 764 to 816 cm^{-1}, owing to the addition of more electronegative O atoms in the network [47].

The FTIR absorption spectrum of the SiO_2-like film is characterized by an intense Si-O-Si mode (rocking), centered at ~440 cm^{-1}: a Si-O mode (bending) located at ~815 cm^{-1}, and an intense Si-O vibration mode (stretching) at ~1100 cm^{-1}. The hydrogen-related vibration modes for C-H and O-H are observed at, respectively, ~2900 cm^{-1} and in the 3100–3700-cm^{-1} range.

The findings outlined above describe the evolution of the as-deposited films from silicon carbide-like to silicon dioxide-like films as the amount of C decreases. Regarding the annealed samples up to 700°C, the IR absorption behavior remains similar to the case of their as-deposited counterparts, and it is worth mentioning that changes took place at annealing temperatures beyond 900°C [44–46].

In the case of the SiC-like sample annealed at 900°C (**Figure 4a**), the Si-C- and Si-O-stretching modes show minor changes. However, both hydrogen-related modes appear with reduced intensities, as expected from the NRA results shown in **Figure 1b**. After the 1100°C annealing, the Si-C absorption band increased drastically in intensity and its line shape changed from Gaussian to mix of Gaussian and Lorentzian, suggesting the presence of longer-range order (Lorentzian). Additionally, all hydrogen-related vibration modes are no longer present in the films owing to hydrogen desorption.

Similarly, for the 900°C-annealed Si-C-O a small intensity increase of the Si-C-stretching mode was observed, while further annealing at 1100°C led to an overall absorption intensity increase accompanied with a blue shift of the Si-O stretching (**Figure 4b**). Finally, the annealing studies on the SiO_2-like material (**Figure 4c**) revealed a significant intensity increase of the Si-O-Si-rocking and the Si-O-stretching modes.

The bond density is directly proportional to the area of the IR band absorption, and can be estimated as in reference [37] using the inverse absorption cross section found in literature (3×10^{19} cm^{-2} for Si-C [48], 1.4×10^{20} cm^{-2} for Si-H [49], and 1.35×10^{21} cm^{-2} for C-H [50, 51]). The Si-C bond density for the as-deposited SiC-like sample is ~2.2×10^{23} cm^{-3} while for the as-deposited Si-C-O sample is ~5.5×10^{22} cm^{-3}. The dependence of Si-C bond density with annealing temperature for both SiC-like and Si-C-O is presented in **Figure 5a**. It shows a constant concentration up to 700°C annealing temperature. At higher temperatures, the Si-C bond concentration increases owing to the densification of the materials and hydrogen desorption, which contributes to the increased availability of Si and C atoms formerly bonded to hydrogen. Indeed, as seen in **Figure 5b**, the bond density of the Si-H and C-H bonds decreases with annealing temperature $T_a \geq 900$°C for both classes of materials.

As shown in **Figure 5c**, the total concentration of hydrogen atoms as determined by the NRA measurements is greater than the total content of hydrogen as calculated by FTIR. Each H-related bond corresponds to one H atom; therefore, the H-related bond density corresponds to the H atomic density. The total atomic density is determined by RBS measurements. This finding suggests that some H atoms are incorporated during CVD growth and are not chemically bound to other elements. These non-bonded H atoms may be present in the form of molecular hydrogen formed during the decomposition of the precursor [37].

3.2. FTIR characterization of silicon oxycarbide nanowires

Large SiC_xO_y NW structures were fabricated on intrinsic Si substrates in order to perform bonding configuration analysis [22]. The normalized absorbance FTIR spectra of both the as-deposited $SiC_{0.34}O_{1.52}$ thin film and the as-fabricated NWs are shown in **Figure 6**. It was found that the bonding configuration of the $SiC_{0.34}O_{1.52}$ NW system was maintained after nanofabrication as the relative intensities of Si-C and Si-O absorption bands remained the

http://dx.doi.org/10.5772/66992

same with respect to the as-deposited thin film. A slight absorption increase of the Si-O shoulder at ~1200 cm^{-1} may be due to surface oxidation induced on the as-synthesized NWs.

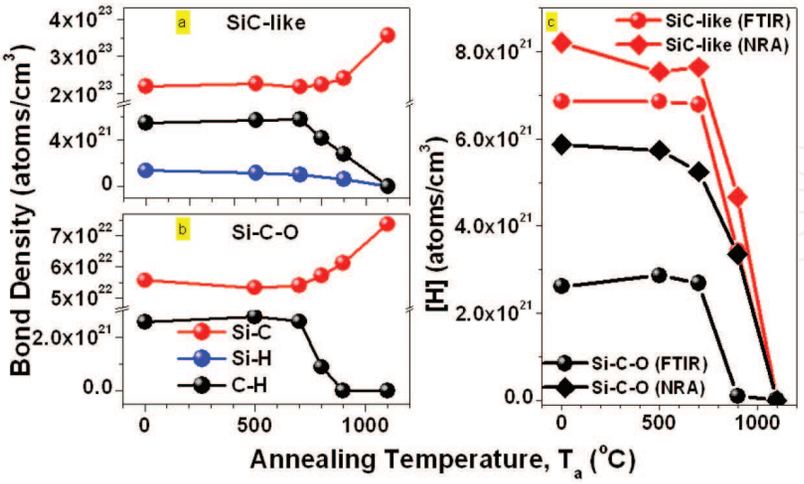

Figure 5. (a) Bond density of Si-C, Si-H, and C-H bonds as a function of annealing temperature for the SiC-like films, (b) bond density of Si-C and C-H bonds as a function of annealing temperature for the Si-C-O films and (c) total atomic concentration of H, as obtained by means of NRA and FTIR for the SiC-like and Si-C-O samples [37].

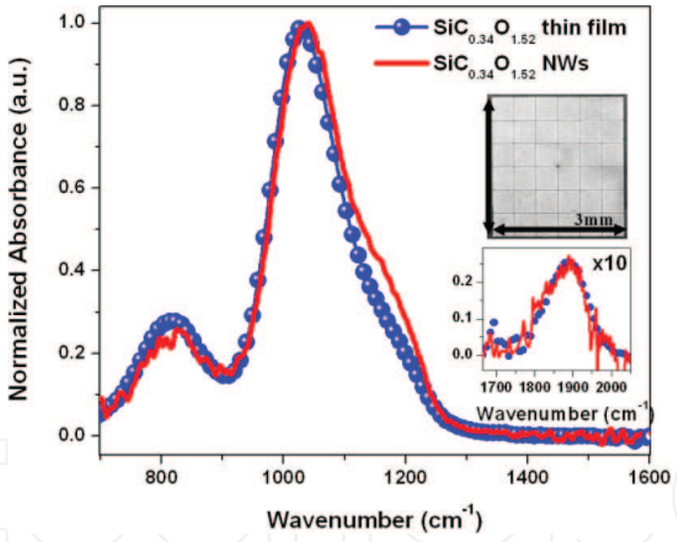

Figure 6. FTIR absorbance spectra of $SiC_{0.34}O_{1.52}$ thin film and its 70-nm-width NW array counterpart. Upper inset: SEM image of the NW array used for FTIR measurements (36 blocks of 490 × 490 μm^2 NW arrays). Lower inset: The conservation of the structural characteristics is also observed in the C=O vibration mode at ~1900 cm^{-1}, which remained unchanged [22].

3.3. XPS characterization of silicon oxycarbide thin films

The information about the bonding configuration in silicon oxycarbide thin films extracted by the means of FTIR analysis was also independently assessed by XPS studies [37]. The XPS analysis focused on examining the electronic environment (chemical bonding) of the Si 2p, C 1s, and O 1s core energy.

In the case of the as-deposited samples, the Si 2p spectrum of the SiC-like matrix (**Figure 7**) is composed of a center peak at 100.3 eV assigned to Si-C bonds and two shoulders centered at 99.2 and 101.2 eV assigned to Si-H- and Si-C-O-type bonding [37, 52]. In the case of the Si-C-O material, the Si 2p peak broadened and shifted to higher binding energies. The peak deconvolution showed the presence of three components centered at 100.8, 102.1, and 103.2 eV which are attributed to the Si-C, Si-C-O, and Si-O bonds, respectively [37, 46, 52]. This result agrees with the FTIR findings where, for both Si-C- and Si-O-stretching modes, the vibration frequencies increased with increasing O content (incorporation of more electronegative atom).

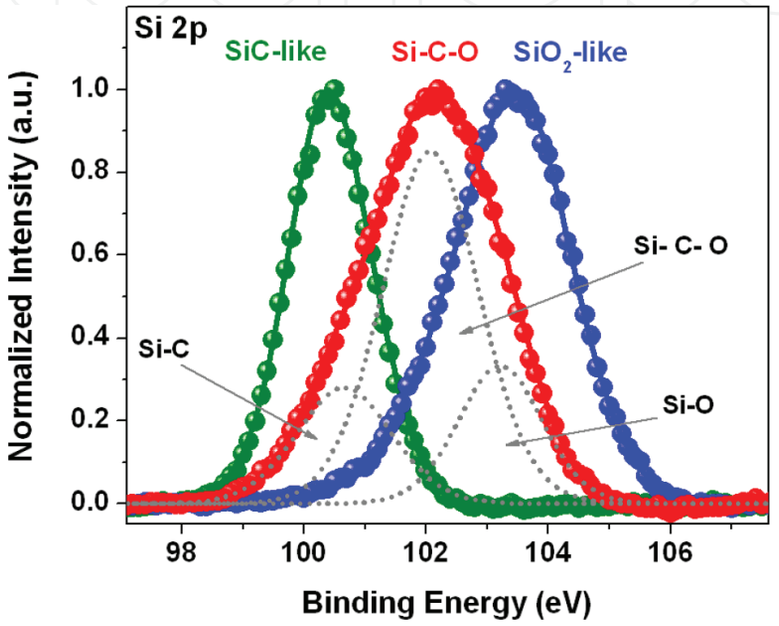

Figure 7. XPS spectra of the Si 2p peaks for the as-deposited SiC-like, Si-C-O and SiO_2-like samples [37].

In the case of the as-deposited SiO_2-like material, the Si 2p spectrum shifted to even higher binding energy and yielded two peaks centered at 102.3 and 103.5 eV which are related to two different Si-O electronic configurations [37, 53, 54].

4. Optical properties of silicon oxycarbide materials

The structural evolution of the as-deposited silicon oxycarbide materials along the $SiC_xO_{2(1-x)}$ stoichiometry was also reflected in their optical properties. The evolution of the index of refraction and the optical gap as a function of the C content of the materials and upon annealing treatments will be addressed in the following subsections.

4.1. Refractive index

The refractive index (n) of SiC_xO_y is found to exhibit a linear relationship with increasing the [Si-C]/[Si-O] bond area ratio (**Figure 8a**). The linear increase of n versus [Si-C]/[Si-O] over the

http://dx.doi.org/10.5772/66992

range analyzed is found to be partly associated with an increase of mass density in SiC_xO_y with increasing [Si-C]/[Si-O] [37]. To understand this behavior, someone can correlate the refractive index (n) or the dielectric constant ($\varepsilon = n^2$) with the structural parameters through the Lorentz-Lorenz (*L-L*) equation [55].

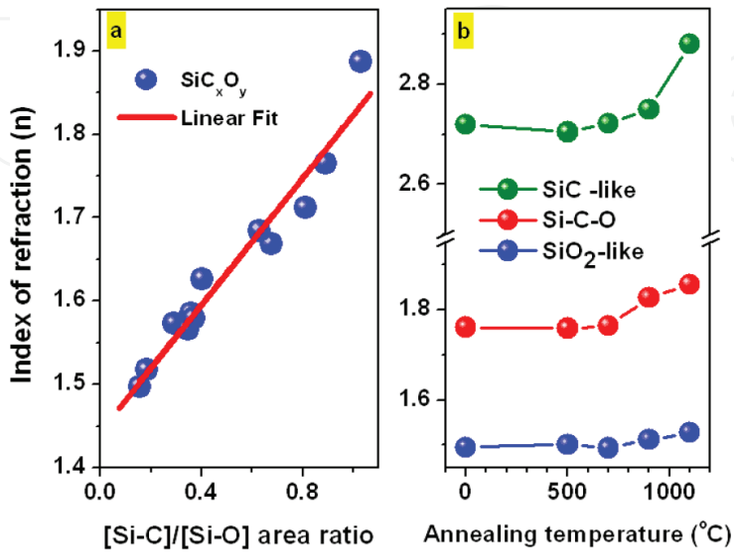

Figure 8. (a) The index of refraction at 800 nm of different SiC_xO_y given as a function of the [Si-C]/[Si-O] bond-area ratio. The solid line is the linear fit of the displayed data and (b) plot of index of refraction (n) at 800 nm as a function of annealing temperature [22, 37].

The FTIR measurements in **Figure 3** show a decrease in the Si-O-Si bond angle with C addition, which is expected considering the difference in the electronegativity between C and O. The mass density and Si atomic content (Si atoms possess higher electronic polarizability than O) of samples with higher carbon concentration is larger as opposed to SiO_2-like samples [56]. It is therefore suggested that the increased index of refraction with increasing [Si-C]/[Si-O] ratio is due to the variations in bond angles, larger mass density, and higher Si content. Further increase of the refractive index of all three classes of silicon oxycarbide materials is also observed upon post-deposition annealing beyond 900°C (**Figure 8b**). This behavior is expected considering the densification of SiC_xO_y materials upon annealing as shown in **Figure 1c** [22, 37].

4.2. Optical gap

The observed increase in the refractive index n, as C concentration increases along the $SiC_xO_{2(1-x)}$ stoichiometry, correlates well with the decrease in the optical gap of the films. For example, the E_{04} gap, which corresponds to the energy where the absorption coefficient (α) is equal to 10^4 cm^{-1} ($\alpha(E_{04}) = 10^4$ cm^{-1}), is found to decrease with increasing [Si-C]/[Si-O] ratio (**Figure 9a**). The Tauc optical gaps, E_g, were also calculated from the optical absorption measurements using Tauc's law, $(\alpha h\nu)^{1/2} = B^{1/2}(h\nu - E_g)$, where α is the absorption coefficient and $h\nu$ is the photon energy [38].

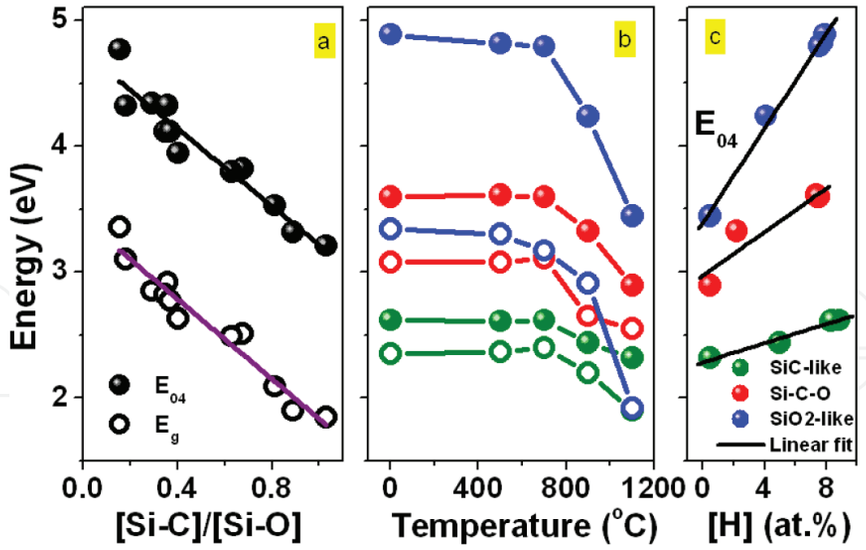

Figure 9. (a) E_{04} and E_g energy values for different SiC_xO_y materials versus the [Si-C]/[Si-O] bond-area ratio, (b) E_{04} (spheres) and E_g (circles) values with annealing temperature and (c) E_{04} values as a function of H content in the films [22, 37].

Similar to E_{04}, the E_g values decrease with increasing [Si-C]/[Si-O]. This behavior can be explained by considering the larger splitting energy difference between the bonding and anti-bonding electronic states in Si-O bonds in comparison to Si-C bonds [22, 38, 57].

In addition, as seen in **Figure 9a**, E_{04} values are generally higher than their E_g counterparts, similar to other hydrogenated disordered systems [58]. This could be explained by taking into account that Tauc's optical gap refers to the optical transitions between extended states close to the band edge, while E_{04} is related to transitions of the extended states away from the band edge [38, 58].

As seen in **Figure 9b**, both the E_{04} and E_g gaps decrease with increasing annealing temperature. It is worth mentioning that the decrease in the optical gap is more pronounced in the films with higher O concentration. For example, the decrease of the Tauc gap values between the as-deposited and post-1100°C annealed films are ~0.5, ~0.6, and ~1.4 eV for, respectively, the SiC-like, Si-C-O, and SiO_2-like classes of SiC_xO_y. It is suspected that the possible precipitation of carbon in the high O-containing systems could be responsible for this phenomenon at high annealing temperatures. The Si-C bond length (~1.88 Å) is longer than the Si-O bond length (~1.63 Å). Consequently, a high degree of strain may accumulate in the Si-C sites within the SiO_2 network (e.g., in the SiO_2-like sample with <5 at.% C). Thermal annealing may result in strain relaxation, with the subsequent structural rearrangements perhaps favoring the formation of carbon clusters, as reported in a previous study [59]. Their optical gap values may vary between ~0.6 and 3 eV, depending on the cluster size [58, 60]. Consequently, it would be expected that the precipitation of carbon in O-rich samples (e.g., SiO_2-like) could be relatively facile, with the optical gap in these samples decreasing more rapidly with increased annealing temperatures.

Furthermore, the decrease in optical gap with increased annealing temperatures seems to correlate well with the loss of hydrogen. As seen in **Figure 9c**, hydrogen reduction is accompanied by

a decrease in the energy band gap in the annealed SiC_xO_y films. The presence of Si-H bonds (~2000 cm^{-1}) can be an indication of dangling-bond passivation in the material, while the presence of other hydrogen-bonding configurations may be responsible for forming recombination centers and increasing the degree of structural disorder [61, 62].

In the as-deposited high C content samples, the Si-H_n stretching mode is found at ~2100 cm^{-1} (insets of **Figure 4**(**a**–**c**)). These peaks are attributed to Si-H-related bonds [63, 64]. Considering the absence of any Si-H_n bonding (2000–2200 cm^{-1}) in the Si-C-O- and SiO_2-like samples, it is suggested that any dangling bonds in the films remained unsaturated, resulting in enhanced structural disorder. Furthermore, hydrogen desorption upon annealing would likely contribute to the formation of additional dangling bonds and defect states, which lead to the increased density of localized states below the mobility edge, thereby decreasing the optical gap. This mechanism seems to be taking place in all thermally grown CVD SiC_xO_y films in this study.

4.3. Structural disorder and dangling bonds

Regarding the electronic structure of amorphous materials, it is common to expect the presence of band-tail states and localized defect states. These states exist due to the structural disorder in materials and may have a significant effect on the material's performance even at low concentrations. Therefore, it is important to elaborate on the degree and impact of structural disorder in the CVD-grown SiC_xO_y systems.

As it was discussed earlier, thermal annealing causes lowering of the optical gap owing to the increased optical absorption observed in the SiC_xO_y materials grown by CVD. The latter is true even at photon energies well below the optical gaps. The enhanced sub-band-gap absorption is a result of an increased density of band-tail states and localized defect states [31]. One of the proposed mechanisms responsible for the increased density of band-tail states upon annealing is the annealing-induced enhanced bond-angle disorder due to structural reconfiguration and/or strain relaxation [65]. In this context, the FTIR full-width half maximum (FWHM) values for both the Si-O- and Si-C-stretching modes in the TCVD SiC_xO_y films, with the exception of the 1100°C-annealed SiC-like sample, increased after annealing, suggesting that thermal treatments indeed enhance bond-angle distortion (see **Figure 4**(**b** and **c**)).

In the case of SiC-like material annealed at 1100°C, the FTIR spectrum shown in **Figure 4a** suggests that a significant amount of crystallization takes place resulting in the Lorentzian line shape of the infrared absorption band. This suggests that the bond-angle disorder is dramatically reduced. However, the optical absorption for the SiC-like films annealed at 1100°C is further increased compared to its as-deposited counterparts [38]. This suggests that, in addition to bond-angle variation, a different type of disorder is also present. Such behavior is known for amorphous covalent materials where both topological and compositional disorders are present simultaneously [66].

Furthermore, the deviation of the CVD-grown SiC_xO_y films from the purely stoichiometric $SiC_xO_{2(1-x)}$ shown in the ternary diagram of **Figure 1** suggests that there is a small excess of carbon that can form homonuclear bonds upon annealing. Also, this deviation increases for

high C concentration materials, toward the SiC-like class regime. The electronic states associated with the homonuclear bonds would exist as localized states within the gap due to their relatively weak bond strength [67, 68].

In this context, electron paramagnetic resonance (EPR) studies on SiC_xO_y materials, grown by CVD, showed the presence of unpaired electrons (dangling bonds) [5]. The same study proposed that one of the major EPR signals may be originated from $(\equiv Si\text{-})_3C^{\bullet}$ radicals or associated defects with different backbone atoms bonded to C atom, such as in C-Si-O configuration [69]. The $SiC_xO_{2(1-x)}$ stoichiometry trend of SiC_xO_y ($SiC_xO_{2(1-x)}$) suggests that two divalent oxygen atoms are replaced by one tetravalent C, further supporting the presence of $(\equiv Si\text{-})_3C^{\bullet}$ radicals in our films, originating from oxygen incorporation into $(\equiv Si\text{-})_4C$ structures. Consequently, the density of such radicals is expected to increase following thermal oxidation of $(\equiv Si\text{-})_{4-n}CH_n$ groups, as it was observed, which have not been completely dehydrated during the film deposition [70]. Similarly, the oxidation of $(\equiv Si\text{-})_{4-n}CH_n$ groups with one or two back-bonded C atoms to Si may also lead to an increased density of Si-dangling bonds in SiC_xO_y. Such dangling bonds may also contribute to the formation of band-tail states in SiC_xO_y [5].

5. Photoluminescence properties of silicon oxycarbide thin films and nanowires

5.1. Visible luminescence emission from SiC_xO_y thin films

The room-temperature photoluminescence spectra for SiC_xO_y samples with different C concentrations under excitation at 300 nm are shown in **Figure 10a**. The spectra are characterized by a broad emission in the whole visible range (350–800 nm). The photoluminescence excitation (PLE) intensity (**Figure 10b**) shows the presence of a shoulder at low excitation energies (<3.5 eV) and a steep increase at high excitation energies (>~3.7 eV). This was fit linearly and the intercept of the fitted line at the photon energy abscissa was taken as the *PLE edge*. As shown in **Figure 10c**, a strong correlation was observed between the values of E_{04} and the PLE edge, suggesting that the PL emission energy in the SiC_xO_y samples may be related to their optical gap [5].

Based on optical, FTIR characterizations, passivation experiments and electron paramagnetic resonance measurements, defect-related mechanisms and small sp^2-carbon clusters that could be attributed to white luminescence from SiC_xO_y thin films were excluded [3, 5]. For example, structural defects typical seen with EPR measurements in silicon oxides, which cannot be explicitly controlled by material processing and are not directly related to the stoichiometry and material characteristics, such as Si-related neutral oxygen vacancies or non-bridging oxygen-hole centers, were ruled out. Instead, the observed intense white luminescence originates from the recombination of photogenerated carriers between the energy bands and at their tail states associated with the Si-O-C/Si-C bonds, as indicated by the direct correlation between the integrated luminescence intensity and the Si-O-C bond density (see **Figure 11**) [3].

http://dx.doi.org/10.5772/66992

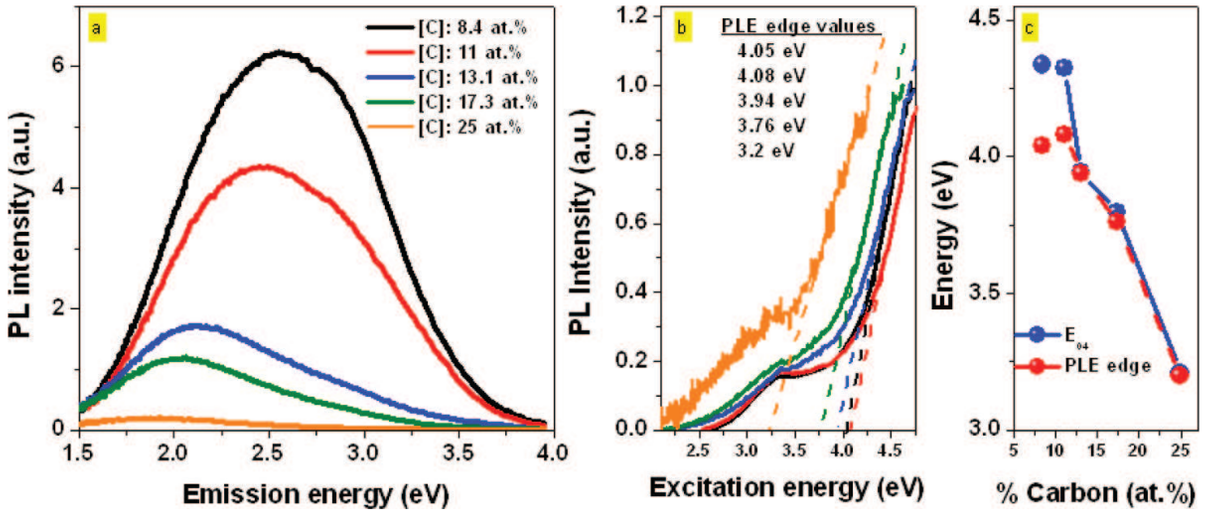

Figure 10. (a) PL emission spectra from as-deposited (AD) SiC_xO_y thin films (4.13 eV excitation, ~300 μW), (b) normalized PLE spectra of the AD SiC_xO_y samples at the PL maxima. The linear fits (dashed lines) of the steep increase of the PLE intensities are shown along with the intercept of these straight lines at the excitation energy (PLE-edge values), and (c) E_{04} and PLE-edge energy values of SiC_xO_y thin films versus C [5].

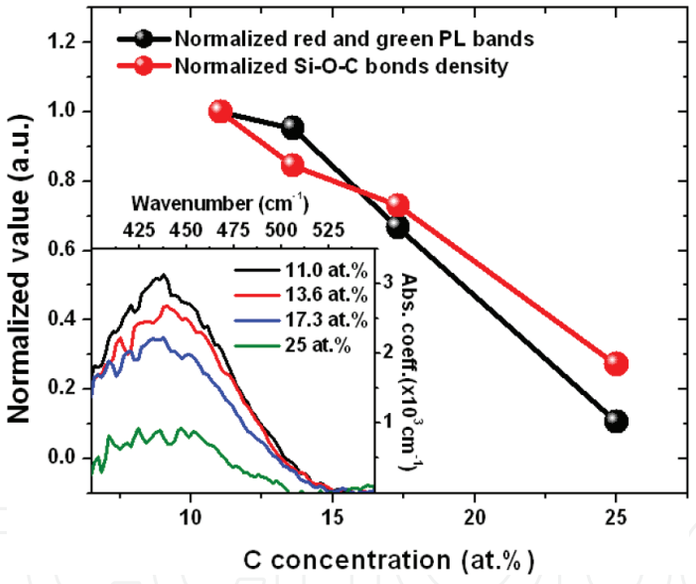

Figure 11. Normalized integrated red and green PL emission bands and the integrated FTIR absorption of Si-O-C functional group at ~440 cm^{-1}. Inset: FTIR absorptions of the Si-O-C-rocking mode in film [5].

On this, the integrated red and green PL emission bands were added and their normalized integrated values were plotted along with the intensity of the red-shifted Si-O-rocking (related to Si-O-C bond density) mode as a function of C content (**Figure 11**) [3]. A strong correlation between the emitted luminescence and the Si-O-C bond density in SiC_xO_y was revealed. This suggests that the emitted luminescence can be directly associated with the Si-O-C structure in the materials [5]. Additionally, the PL/PLE analysis revealed a strong similarity in the PLE behavior for the green/blue band emissions between the SiC control and SiC_xO_y, suggesting

that C-Si/C-Si-O bonding may be also responsible for the excitation path of the observed luminescence in SiC_xO_y.

5.2. Band-tail recombination model

Representative forming gas-annealed SiC_xO_y samples were additionally studied with means of PL and PLE analyses as presented in **Figure 12** [22].

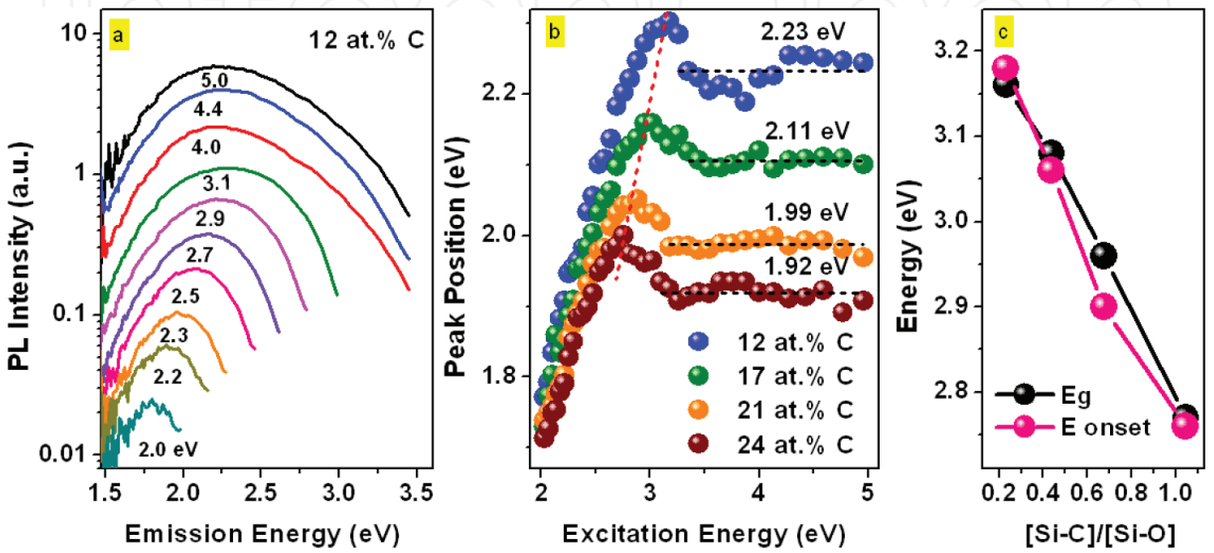

Figure 12. (a) Steady-state PL of the FG-annealed SiC_xO_y with 12 at.% *C* content ($SiC_{0.34}O_{1.52}$) under varying excitation photon energies (E_{exc}). The PL intensity increased monotonically by two orders of magnitude with E_{exc}, suggesting that the efficiency of photo-carrier generation increases with E_{exc}, (b) room-temperature steady-state PL peak position dependence on excitation energy of SiC_xO_y thin films of varying carbon concentrations. With increase in excitation energy, the PL peak-emission-position blue-shifts until ~$E_{exc,on}$ (red-dotted line is used as a guide to the eye). Hopping edges are indicated by horizontal black dotted lines and (c) E_g calculated from Tauc's law and $E_{exc,on}$ values as a function of [Si-C]/[Si-O] bond ratio [23].

The evolution of the PL peak position in SiC_xO_y was supported by the band-tail states recombination model, typical of amorphous materials [71]. Upon excitation, the photogenerated carriers thermalized to lower energies associated with band edges (hopping edge) before they recombined radiatively (energy plateau in **Figure 12b**). The PL peak position increased with the excitation energy up to the $E_{exc,on}$ value, as the electron population at high-lying band-tail levels of the conduction band increasing with higher excitation energy. The red shift of $E_{exc,on}$ seen with increasing C content in SiC_xO_y can be ascribed to the observed linear decrease of the optical gap (E_g) with increasing [Si-C]/[Si-O] and their values almost coincide with the E_g values of the films [22].

PL dynamics experiments showed a fast decrease of the PL intensity, suggesting the existence of fast recombination mechanisms in SiC_xO_y, and the PL decay spectra followed a stretched exponential law [23]. These findings further support a band-tail states recombination model, in which carriers recombine by tunneling between spatially separated conduction and valence band-tail states. Due to the diffusivity/tunneling of the photogenerated carriers during thermalization in the band-tail states before they recombine and the inhomogeneous

http://dx.doi.org/10.5772/66992

constitution of the band-tail states related to C-Si/Si-O-C bonding, where each state contributes with a slightly different PL lifetime, a distribution of lifetimes is expected, hence the stretched exponential behavior. This is inherent in disordered semiconductors, such as amorphous Si:H, C:H, SiC_x, and SiN_x, due to the broad and variable spatial density of these states [72–74].

To further elucidate on the band-tail states recombination model in SiC_xO_y, the PL luminescence decay at different emission energies was additionally investigated. The time evolution of the PL line shape is presented in **Figure 13a**. It can be seen that during the first 1 ns of the luminescence decay, the integrated intensity substantially decreased and a red shift, equal to $\Delta E = 0.31$ eV, in the PL emission peaks occurs for the SiC_xO_y thin film with 12 at.% C. This red shift is found to be less for samples with higher C concentration [23].

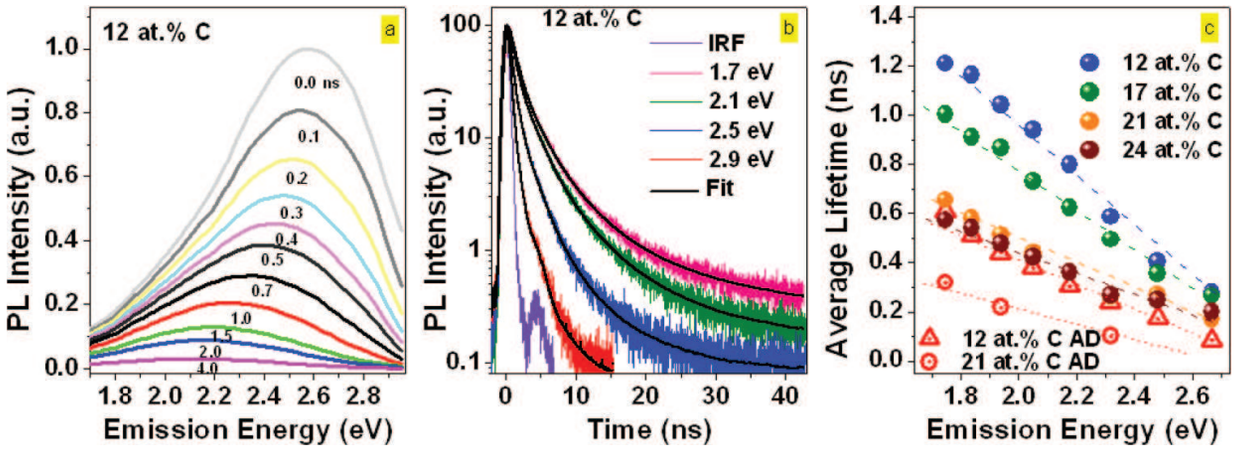

Figure 13. (a) Time evolution of PL spectrum of $SiC_{0.34}O_{1.52}$ (E_{exc} = 3.06 eV). The number associated with each spectrum indicates the elapsed time (in nanoseconds) after excitation. (b) Raw data of PL decay transients of $SiC_{0.34}O_{1.52}$ film at different emission energies (IRF in black). (c) Average lifetimes of FG-annealed SiC_xO_y films with different *C* contents at different emission energies. The average lifetimes of the as-deposited (AD) SiC_xO_y films with 12 at.% C and 21 at.% C are also shown (gray symbols) [23].

Furthermore, the PL lifetimes increased as the emission energy was decreased, in agreement with electron-hole (e-h) hopping within lower-energy tail states, as the rate of thermalization decreases significantly due to the rapidly decreasing density of band-tail states [75]. Similar behavior was observed in amorphous semiconductors where the luminescence lifetime increase is attributed to e-h hopping [74]. Upon FG annealing, the average lifetimes exhibited higher values compared to their as-deposited counterparts (**Figure 13c**). Furthermore, the integrated PL intensity of the FG-annealed films increased significantly along with a blue shift in peak position (e.g., six times for the sample with 21 at.% C with 0.2 eV blue shift). This change in lifetimes and PL intensity can be attributed primarily to the passivation of non-radiative recombination centers present in lower-energy portion of the band-tail states of the as-deposited films.

The increase in the luminescence lifetime in SiC_xO_y with low *C* content can be attributed to the decrease of non-radiative recombination paths compared to their high *C* content counterparts. As the SiC_xO_y composition evolves from SiC-like to SiO_2-like, a decrease of the local disorder is

expected. As presented above herein FTIR measurements suggest that the degree of bond-angle disorder decreases with decreasing *C* content in the chemically grown SiC_xO_y films.

Additionally, it is expected that in the case of high *C* content samples, the density of band-tail states should increase as indicated by their increased sub-bandgap absorption [15, 76]. Therefore, for SiC_xO_y films with higher *C* content (*C* >14 at.%), a higher density of band-tail states and enhanced disorder is expected, which results in faster thermalization of the photogenerated carriers yielding higher decay rates and a tighter lifetime distribution (**Figure 13b**) [23].

5.3. Visible luminescence from SiC_xO_y nanowires

Figure 14a and **b** shows the normalized room-temperature PLE and PL emission spectra of $SiC_{0.34}O_{1.52}$ nanowire arrays. To better understand the visible light emission in SiC_xO_y NWs, their PL and PLE properties were explored in conjunction with data from the thin film of the same composition. The PL emission spectrum of $SiC_{0.34}O_{1.52}$ NWs exhibits broadband characteristics ranging from blue to deep red, while the PLE spectrum monitored at the peak luminescence emission (~550-nm) spans from near-UV to blue/green regions of the spectrum.

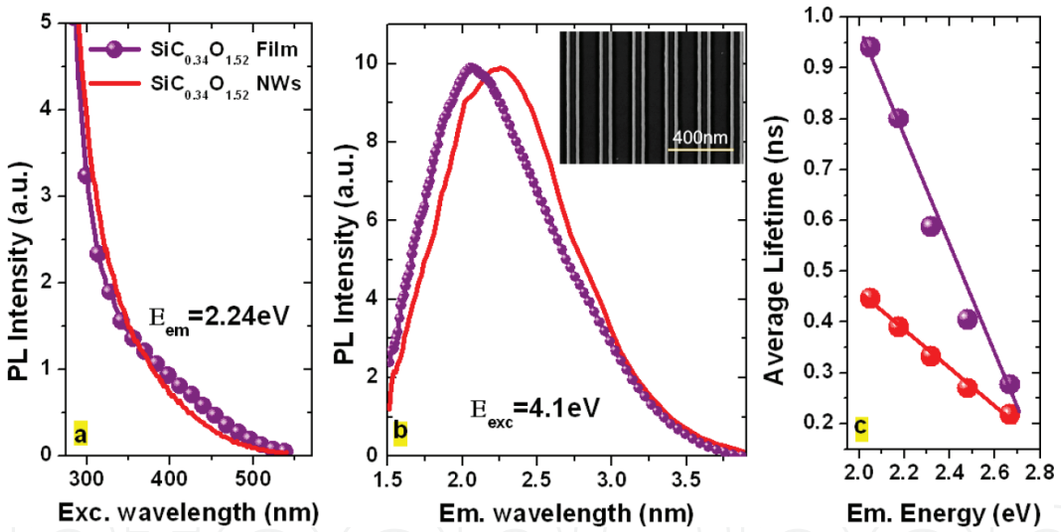

Figure 14. (a) Room-temperature PLE spectra of 120-nm-thick $SiC_{0.34}O_{1.52}$ thin film and its corresponding NWs measured at its emission peak. Almost identical PLE emission spectra between NWs and thin films were observed, suggesting that there is no change in the excitation path and emission origin of the observed luminescence in $SiC_{0.34}O_{1.52}$ nanowires, (b) ensemble steady-state normalized PL spectrum of the SiC_xO_y NWs array along with the normalized PL spectrum of its thin film analog (E_{exc} = 4.1 eV) and (c) average lifetimes of the SiC_xO_y NW array with 12 at.% C and its thin film analog at different PL emission energies [22, 23].

PLE analysis suggested that the observed luminescence from SiC_xO_y NWs is related to radiative recombination of photo-excited carriers in band-tail states associated with C-Si/Si-O-C-bonding groups [5, 22]. Furthermore, a supplementary mechanism, in addition to the proposed band-tail states recombination process, may be needed in order to take into account the reduced dimensionality of SiC_xO_y NW. In the case of the NW structure with spatially confined volume, the statistics of the lowest energy states due to Si-C bonds may be excluded [77]. Furthermore, by nanostructuring the recombination volume is reduced, thus, the tunneling

http://dx.doi.org/10.5772/66992

probability of a carrier between adjacent states at similar energy is expected to decrease. Consequently, the carriers will be exposed to a smaller number of non-radiative sites [23, 77, 78], resulting in enhanced PL efficiency, PL blue shift, and faster lifetimes with a tighter distribution as observed in $SiC_{0.34}O_{1.52}$ (12 at.% C) (**Figure 14c**). However, it is important to emphasize that the effects of NW-related surface recombination and optical scattering may not be ruled out.

5.4. Photo-stability upon thermal oxidation and excitation power density

In addition to PL and PLE studies, the luminescence performance of the $SiC_{0.34}O_{1.52}$ NW arrays was investigated as a function of oxidation temperature and excitation power density [22].

The oxidation treatments up to 250°C (**Figure 15a**) did not cause any change in the composition and bonding configuration of the $SiC_{0.34}O_{1.52}$ material. Consequently, the emission intensity and line shape, from $SiC_{0.34}O_{1.52}$ nanostructured arrays, did not reveal any changes, suggesting the absence of luminescence degradation due to thermal oxidation. This stability can be attributed to the similarity of the oxidation rates and activation energies of SiC_xO_y materials to those of SiC [79]. Hence, SiC_xO_y materials (with higher carbon content) appear to be significantly more resistant to oxidation annealing, compared to its SiO_2-like counterparts (with very low carbon content) [3].

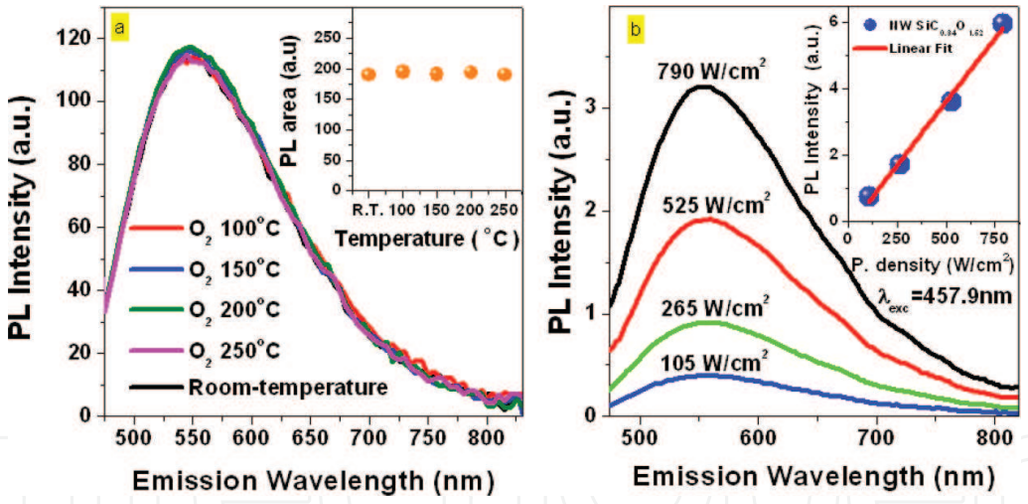

Figure 15. (a) PL spectra of the AD and 2-h-oxygen-annealed $SiC_{0.34}O_{1.52}$ NW at various temperatures (excitation wavelength λ_{exc} = 457 nm). The inset shows the integrated PL intensity versus annealing temperature and (b) room-temperature PL spectra of the 70-nm-width $SiC_{0.34}O_{1.52}$ NWs for different CW excitation probing power densities (excited at the λ_{exc} = 457.9 nm of an Ar ion laser). The inset shows the linear behavior of the integrated PL intensity as a function of the excitation power density [22].

The excitation power dependence study (**Figure 15b**) showed a linear behavior in the integrated PL with respect to the power density (up to ~800 W/cm^2). Similar to the thermal-oxidation study, the peak position and the line shape of the PL in the nanowires remained unchanged, suggesting good emission stability at high excitation intensity [22]. The latter is more supporting evidence suggesting the absence of defect-related localized emission in the proposed origin of the visible luminescence from SiC_xO_y nanowires, as no PL saturation at high powers was observed (e.g., due to state filling of the localized states) [80, 81].

6. Concluding remarks

The optical and luminescence properties of silicon oxycarbide thin films and nanostructured (e.g., NW) arrays are correlated to their synthesis routes, structural properties, and bonding configuration. The composition of the chemically CVD-grown SiC_xO_y thin films approximate the $SiC_xO_{2(1-x)}$ ($0 < x < 1$) stoichiometry. The index of refraction increases linearly as the [Si–C]/[Si–O] bond-area ratio increases, accompanied by a linear decrease of the optical gap. The white (red, green, and blue) emission can be achieved simultaneously from the same SiC_xO_y film following a single-deposition process, without the complications encountered in the case of using nanocrystals (e.g., Si, SiC). In particular, it was determined that the white PL emission of SiC_xO_y thin films is strong enough to be seen with the naked eye under bright room conditions. Based on the PL, FTIR, and EPR analyses, typical structural defects in oxides were ruled out as the mechanism for white luminescence from SiC_xO_y. Instead, the observed intense visible luminescence originates from the recombination of photo-generated carriers between the energy bands and at their tail states associated with Si-O-C/Si-C bonds. In this regard, the potential advantages offered by our proposed approach of SiC_xO_y thin films and NWs range from color tunability, thermal/photo-stability to enhanced light extraction efficiency and from cost reduction to environmental considerations. To this end, these compelling behaviors may provide a pathway for further controlling and enhancing the thermal stability and PL yield of white light emission from such films and nanostructured materials through optimal engineering of Si-O-C/Si-C bonds in the matrix.

Acknowledgements

The authors would like to thank Dr. Mengbing Huang, of the Colleges of Nanoscale Sciences and Engineering at SUNY POLY, for his contribution to the work presented herein.

Author details

Spyros Gallis*, Vasileios Nikas and Alain E. Kaloyeros

*Address all correspondence to: sgalis@sunypoly.edu

Colleges of Nanoscale Sciences and Engineering, SUNY Polytechnic Institute, Albany, NY, USA

References

[1] Grill A., Gates S. M., Ryan T. E., Nguyen S. V., and Priyadarshini D. Progress in the development and understanding of advanced low k and ultralow k dielectrics for very large-scale integrated interconnects-State of the art. Applied Physics Review 2014;1:011306.

[2] King S. W. Dielectric barrier, etch stop, and metal capping materials for state of the art and beyond metal interconnects. ECS Journal of Solid State Science and Technology 2015;4:N3029.

[3] Gallis S., Nikas V., Suhag H., Huang M., and Kaloyeros A. E. White light emission from amorphous silicon oxycarbide (a-SiC_xO_y) thin films: Role of composition and post-deposition annealing. Applied Physics Letters 2010;97:081905.

[4] Vasin A. V. Structural and luminescent properties of carbonized silicon oxide thin layers. In Nazarov A., Balestra F, Valeriya K, Flandre D. (ed) Functional Nanomaterials and Devices for Electronics, Sensors and Energy Harvesting Engineering Materials. Springer, Cham, Heidelberg, New York, Dordrecht, London; Switzerland, Germany, United States of America, The Netherlands, United Kingdom; 2014, p. 297.

[5] Nikas V., Gallis S., Nguyen A. P. D., Stesmans A., Afanas'ev V. V. and Kaloyeros A. E. The origin of white luminescence from silicon oxycarbide thin films. Appled Physics Letters 2014;104: 061906.

[6] Tamayo A., Rubio J., Rubio F., Oteo J. L., and Riedel R. Texture and micro-nanostructure of porous silicon oxycarbide glasses prepared from hybrid materials aged in different solvents. Journal of European Ceramics Society 2011;31: 1791.

[7] Kim Y. W., Kim S. H., and Park C. B. Processing of closed-cell silicon oxycarbide foams from a preceramic polymer. Journal of Materials Science 2004;39:5647.

[8] Nghiem Q. D., Cho S. J., and Kim D. P. Synthesis of heat-resistant mesoporous SiOC ceramic and its hydrogen adsorption. Journal of Materials Chemistry 2006;16:558.

[9] Karakuscu A., Ponzoni A., Aravind P. R., Sberveglieri G., and Soraru G. D. Gas sensing behavior of mesoporous SiOC glasses. Journal of American Ceramics Society 2013;96:2366.

[10] Liu X., Xie K., Zheng C.M, Wang J., and Jing Z. Q. Si-O-C materials prepared with a sol–gel method for negative electrode of lithium battery. Power Sources 2012;214:119.

[11] Bhandavat R., and Singh G. Stable and efficient Li-ion battery anodes prepared from polymer-derived silicon oxycarbide–carbon nanotube shell/core composites. Journal of Physical Chemistry C 2013;117:11899.

[12] Zhuo R., Colombo P, Pantano C, and Vogler E. A. Silicon oxycarbide glasses for blood-contact applications. Acta Biomaterialia 2005;1:583.

[13] Bellocchi G. Franzò G. Boninelli S., Miritello M., Cesca T., Iacona F. and F Priolo. Structural and luminescence properties of undoped and Eu-doped SiOC thin films. Materials Science and Engineering 2014;56:012009.

[14] Gallis S., Huang M., Efstathiadis H., Eisenbraun E., Nyein E., Hommerich U., and Kaloyeros A. E. Photoluminescence in erbium doped silicon oxycarbide thin films. Applied Physics Letters 2005;87:091901.

[15] Gallis S., Huang M., and Kaloyeros A. E. Efficient energy transfer from silicon oxycarbide matrix to Er ions via indirect excitation mechanisms. Applied Physics Letters 2007;90: 161914.

[16] Nikas V., Gallis S., Huang M., and Kaloyeros A. E. Thermal annealing effects on photoluminescence properties of carbon-doped silicon-rich oxide thin films implanted with erbium. Journal of Applied Physics 2011;109:093521.

[17] Liang D., and Bowers J. E.. Recent progress in lasers on silicon. Nature Photonics 2010;4:511.

[18] Fang Z., Chen Q. Y., and Zhao C. Z. A review of recent progress in lasers on silicon. Optics and Laser Technology 2013;46:103.

[19] Fan S., Villeneuve P.R, Joannopoulos J. D., and Schubert E. F. High Extraction efficiency of spontaneous emission from slabs of photonic crystals. Physical Review Letters 1997;78: 3294.

[20] Guichard A. R., Kekatpure R. D., Brongersma M. L., and Kamins T. I. Temperature-dependent Auger recombination dynamics in luminescent silicon nanowires. Physical Review B 2008;78:235422.

[21] He Y., Fan C., and Lee S. T. Silicon nanostructures for bioapplications. Nano Today 2010;5:282.

[22] Nikas V, Tabassum N., Ford B., Smith L., Kaloyeros A. E., and Gallis S., Strong visible light emission from silicon oxycarbide nanowire arrays prepared by electron beam lithography and reactive ion etching. Journal of Materials Research 2015;30:3692.

[23] Tabassum N., Nikas V., Ford B., Huang M., Kaloyeros A. E., and Gallis S. Time resolved analysis of the white photoluminescence from chemically synthesized SiC_xO_y thin films and nanowires. Applied Physics Letters 2016;109:043104.

[24] Wang Q., Zhang W., Zhong M., Ma J., Wu Z., and Wang G. Synthesis and Photoluminescence of Amorphous Silicon Oxycarbide Nanowires. Chinese Journal of Chemical Physics 2015;28:184.

[25] Zhao Y., Riemersma C., Pietra F., Koole R., Donegá C. M., and Meijerink A. High-temperature luminescence quenching of colloidal quantum dots. ACS Nano 2012;6:9058.

[26] Tayagaki T., Fukatsu S., and Kanemitsu Y. Photoluminescence dynamics and reduced Auger recombination in $Si_{1-x}Ge_x/Si$ superlattices under high-density photoexcitation. Physical Review B 2009;79:041301.

[27] Grill A. Plasma enhanced chemical vapor deposited SiCOH dielectrics: from low-k to extreme low-k interconnect materials. Journal of Applied Physics 2003;93:1785.

[28] Chiang C. C., Chen M. C., Li L. J., Wu Z. C., Jang S. M., and Liang M. S. Physical and barrier properties of amorphous silicon-oxycarbide deposited by PECVD from octamethylcyclotetrasiloxane. Journal of the Electrochemical Society 2004;151(9):G612.

[29] Wang M. R., Rusli, Xie J. L., Babu N., Li C. Y., and Rakesh K. Study of oxygen influences on carbon doped silicon oxide low-k thin films deposited by plasma enhanced chemical vapor deposition. Journal of Applied Physics 2004;96:829.

[30] Kim Y. H., Hwang M. S., Kim H. J., Kim J. Y., and Lee Y. Infrared spectroscopy study of low dielectric-constant fluorine-incorporated and carbon-incorporated silicon oxide films. Journal of Applied Physics 2001;90:3367.

[31] Lin Z., Guo Y, Song J., Zhang Y., Song C, Wang X., Huang R. Effect of thermal annealing on the blue luminescence of amorphous silicon oxycarbide films. Journal of Non-Crystalline Solids 2015;428:184.

[32] Ryan J. V. and Pantano C. G. Synthesis and characterization of inorganic silicon oxycarbide glass thin films by reactive rf-magnetron sputtering. Journal of Vacuum Science & Technology A 2007;25:153.

[33] Vasin A. V., Rusavsky A. V., Kysil D. V., Prucna S., Piryatinsky Y. P., Starik S. P., Nasieka I., Strelchuk V. V., Lysenko V. S., Nazarov A. N. The effect of deposition processing on structural and luminescent properties of a-SiOC:H thin films fabricated by RF-magnetron sputtering. Journal of Luminescence 2016; in press. http://www.sciencedirect.com/science/article/pii/S0022231316314247. http://dx.doi.org/10.1016/j.jlumin.2016.10.029

[34] Karakuscu, A., Guider, R., Pavesi, L., Soraru, G.D.: Broad-band tunable visible emission of sol–gel derived SiBOC ceramic thin films. Thin Solid Films 2011;519:3822.

[35] Abbass A. E., Swart H. C., Kroon R. E. White luminescence from sol–gel silica doped with silver. Journal of Sol–gel Science Technology 2015;76:708.

[36] Vasin A.V., Ishikawa Y., Kolesnik S.P., Konchits A.A., Lysenko V.S., Nazarov A.N., Rudko G. Y. Light-emitting properties of amorphous Si:C:O: H layers fabricated by oxidation of carbon-rich a-Si:C: H films. Solid State Science. 2009;11:1833.

[37] Gallis S., Nikas V., Eisenbraun E., Huang M., and Kaloyeros A. E. On the effects of thermal treatment on the composition, structure, morphology, and optical properties of hydrogenated amorphous silicon-oxycarbide. Journal of Materials Research 2009;24: 2561.

[38] Gallis S., Nikas V., Huang M., Eisenbraun E., and Kaloyeros: A. E. Comparative study of the effects of thermal treatment on the optical properties of hydrogenated amorphous silicon-oxycarbide. Journal of Applied Physics 2007;102:024302.

[39] Bréquel H., Parmentier J., Walter S., Badheka R., Trimmel G., Masse S., Latournerie J., Dempsey P., Turquat C., Chomel A. D., Neindre-Prum L. L., Jayasooriya U. A., Hourlier D., Kleebe H. J, Soraru G. D., Enzo S., and Babonneau F. Systematic structural characterization of the high-temperature behavior of nearly stoichiometric silicon oxycarbide glasses. Chemistry of Materials 2004;16:2585.

[40] Kroll P. Searching insight into the atomistic structure of SiCO ceramics. Journal of Materials Chemistry 2010;20:10528.

[41] Lanford W. A., Trautvetter H. P., Ziegler J. F. and Keller J. New precision technique for measuring the concentration versus depth of hydrogen in solids. Applied Physics Letters 1976;28:566.

[42] Lehmann A., Schumann L., and Hubner K. Optical phonons in amorphous silicon oxides. I. Calculation of the density of states and interpretation of Lo-To splittings of amorphous SiO_2. Physical Status Solidi (b) 1983;117:689.

[43] Wolfe D. M., Hinds B. J., Wang F., Lucovsky G., Ward B. L., Xu M., Nemanich R. J., and Maher D. M. Thermochemical stability of silicon–oxygen–carbon alloy thin films: a model system for chemical and structural relaxation at SiC–SiO_2 interfaces. Journal of Vacuum Science and Technology A 1999;17:2170.

[44] Tolstoy V. P., Chernyshova I. V., and Skryshevsky V. A. Handbook of Infrared Spectroscopy of Ultrathin Films. Wiley; New York; 2003.

[45] Socrates G. Infrared Characteristic Group Frequencies. Wiley: Chichester; 2001.

[46] Besling W. F. A., Goossens A., Meester B., Schoonman J. Laser-induced chemical vapor deposition of nanostructured silicon carbonitride thin films. Journal of Applied Physics 1998;83:544.

[47] Demichellis F., Pirri C. F., and Tresso E. F. Influence of doping on the structural and optoelectronic properties of amorphous and microcrystalline silicon carbide. Journal of Applied Physics 1992;72:1327.

[48] Fang C. F., Gruntz K. J., Ley L., Cardona M., Demond F. J, Müller G., and Kalbitzer S. The hydrogen content of a-Ge:H and a-Si:H as determined by IR spectroscopy, gas evolution and nuclear reaction techniques. Journal of Non-Crystalline Solids 1980;35–36:255.

[49] Basa D. K. and Smith F. W. Annealing and crystallization processes in a hydrogenated amorphous Si-C alloy film. Thin Solid Films 1990;192:121.

[50] Fujimoto F., Ootuka A., Komaki K. I., Iwata Y., Yamane I., Yamashita H., Hashimoto Y., Tawada Y., Nishimura K., Okamoto H. and Hamakawa Y. Hydrogen content in a-SiC:H films prepared by plasma decomposition of silane and methane or ethylene. Japanese Journal of Applied Physics Part 1 1984;23:810.

[51] Nakazawa K., Ueda S., Kumeda M., Morimoto A., and Shimizu T. NMR and IR studies on hydrogenated amorphous $Si_{1-x}C_x$ Films. Japanese Journal of Applied Physics Part 1 1982;21:L176.

[52] Smith K. L., and Black K. M. Characterization of the treated surfaces of silicon alloyed pyrolytic carbon and SiC. Journal of Vacuum Science and Technology A 1984;2:744.

[53] Choi W. K., Ong T. Y., Tan L. S., Loh F. C., Tan K. L. Infrared and x-ray photolectron spectroscopy studies of as-prepared and furnace-annealed radio-frequency sputtered amorphous silicon carbide films. Journal of Applied Physics 1998;83:4968.

[54] Bell, F. G. and Ley L. Photoemission study of SiO_x ($0 \leq x \leq 2$) alloys. Physical Review B 1988;37:8383.

[55] Maex K., Baklanov M. R., Shamiryan D., Iacopi F., Brongersma S. H., Yanovitskaya Z. S. Low dielectric constant materials for microelectronics. Journal of Applied Physics 2003;93:8793.

[56] Dehan E., Temple-Boyer P., Henda R., Pedroviejo J. J. and Scheid E. Optical and structural properties of SiO_x and SiN_x materials. Thin Solid Films 1995;266:14.

[57] Sun C. Q. A model of bonding and band-forming for oxides and nitrides. Applied Physics Letters 1998;72:6.

[58] Carey J. D., Silva S. R. P. Disorder, clustering, and localization effects in amorphous carbon. Physical Review B 2004;70:235417.

[59] Das G., Mariotto G., Quaranta A. Microstructural evolution of thermally treated low-dielectric constant SiOC:H films prepared by PECVD. Journal of the Electrochemical Society 2006;153:F46.

[60] Fanchini G., Tagliaferro A. Disorder and Urbach energy in hydrogenated amorphous carbon: a phenomenological model. Applied Physics Letters 2004;85:730.

[61] Joannopoulos J. D. and Lucovsky G. The Physics of Hydrogenated Amorphous Silicon II. Springer: Berlin; 1984.

[62] Brodsky M. H. Amorphous Semiconductors. Springer-Verlag: Berlin; 1979.

[63] Wagner H., Beyer W. Reinterpretation of the silicon-hydrogen stretch frequencies in amorphous silicon. Solid State Communications 1983;48:585.

[64] Kumbhar A. S., Bhusari D. M., and Kshirsagar S. T. Growth of clean amorphous silicon–carbon alloy films by hot-filament assisted chemical vapor deposition technique. Applied Physics Letters 1995;66:1741.

[65] Musumeci P., Roccaforte F., Reitano R. Angular distortion of Si clusters in a-SiC. Europhysics Letters 2001;55:674.

[66] Compagnini G., Foti G., Makhtari A. Vibrational analysis of compositional disorder in amorphous silicon carbon alloys. Europhysics Letters 1998;41:225.

[67] Ivashchenko V. I., Shevchenko V. I., Rusakov G. V., Klymenko A. S., Popov, Ivashchenko L. A., Bogdanov E. I. Gap states in a-SiC fromoptical measurements and band structure models. Journal of Physics: Condensed Matter 2002;14:1799.

[68] Nguyen-Tran T., Suendo V., Roca P., and Cabarrocas I. Optical study of disorder and defects in hydrogenated amorphous silicon carbon alloys. Applied Physics Letters 2005;87:011903.

[69] Afanas'ev V. V., Nguyen A. P. D., Houssa M., Stesmans A. , Tőkei Z., and Baklanov M. R. High-resolution electron spin resonance analysis of ion bombardment induced defects in advanced low-κ insulators (κ=2.0–2.5). Applied Physics Letters 2013;102:172908.

[70] Trakhtenberg L. I., Lin S. H., and Ilegbusi O. J. Physico-chemical phenomena in thin films and at solid surfaces. Thin Films and Nanostructures 2007;316:314.

[71] Murayama K., Sano W., Ito T., and Ogiwara C. Excitation energy evolution of photoluminescence spectrum in amorphous hydrogenated silicon. Solid State Communications 2008;146:315.

[72] Lormes W., Hundhausen M., and Ley L. Time resolved photoluminescence of amorphous hydrogenated carbon. Journal of Non-Crystalline Solids 1998;227:570.

[73] Pelant I., and Valenta J. Luminescence Spectroscopy of Semiconductors. Oxford: University Press; 2012.

[74] Giorgis F., Mandracci P., Dal Negro L., Mazzoleni M., and Pavesi P. Optical absorption and luminescence properties of wide-band gap amorphous silicon based alloys. Journal of Non-Crystalline Solids 2000;266:588.

[75] Monroe D. Hopping in exponential band tails. Physical Review Letters 1985;54:146.

[76] Tessler L. R., and Solomon I. Photoluminescence of tetrahedrally coordinated *a*-$Si_{1-x}C_x$:H. Physical Review B 1995;52:10962.

[77] Estes M. J., and Moddel G. Luminescence from amorphous silicon nanostructures. Physical Review B 1996;54:14633.

[78] Robertson J. Recombination and photoluminescence mechanism in hydrogenated amorphous carbon. Physical Review B 1996;53:16302.

[79] Chollon G. Oxidation behaviour of ceramic fibres from the Si–C–N–O system and related sub-systems. Journal of European Ceramics Society 2000;20:1959.

[80] Tayagaki T., Fukatsu S., and Kanemitsu Y. Photoluminescence dynamics and reduced Auger recombination in $Si_{1-x}Ge_x$/Si superlattices under high-density photoexcitation. Physical Review B 2009;79:041301.

[81] Grieshaber W., Schubert E. F., Goepfert I. D., Karlicek R. F., Schurman M. J., and Tran C. Competition between band gap and yellow luminescence in GaN and its relevance for optoelectronic devices. Journal of Applied Physics 1996;80:4615.